Capacitive Energy Conversion With Circuits Implementing a Rectangular Charge-Voltage Cycle Part 2: Electromechanical and Nonlinear Analysis

Eoghan O'Riordan, *Student Member, IEEE*, Andrii Dudka, Dimitri Galayko, *Member, IEEE*, Philippe Basset, Orla Feely, *Fellow, IEEE*, and Elena Blokhina, *Senior Member, IEEE*

Abstract—In this paper, we explore and describe the electromechanical coupling which results from eKEH conditioning circuits implementing a rectangular QV cycle, including but not limited to the charge pump and Bennet's doubler circuits. We present numerical and semi-analytical analyses describing the nonlinear relationship between the oscillating mass and the conditioning circuit. We believe this is a poorly understood facet of the device and, as we will portray, affects the potential harvested energy. An approach to determine the frequency shift due to the electromechanical coupling is presented and compared with novel experimental results. We provide some examples of bifurcation behavior and show that the only source of nonlinearity is in the coupling between the electrical and mechanical domains. This work continues from the electrical analysis presented in Part 1, providing a full insight into the complex behavior of the electromechanical coupling.

Index Terms—Bifurcation analysis, electromechanical coupling, electrostatic kinetic energy harvesters, multiple scale methods, steady-state oscillations.

I. INTRODUCTION

A S AN electrostatic kinetic energy harvester (eKEH) is a type of transducer, converting mechanical vibrations into electrical energy [1]–[4], an understanding of the relative effects caused by both physical domains provides a greater insight into how the system operates and so how it may be optimized.

Due to the use of a variable capacitor, eKEHs require an initial biasing. This can be provided in the form of an electret or some power source. In either case, once an electrical bias is placed across the capacitive plates (which oscillate freely with the external mechanical vibrations when unbiased) the eKEH experiences electromechanical coupling.

There are three general families of eKEH conditioning circuits which can be grouped according to the QV cycle they implement: the tear drop QV cycle [5], [6], triangular QV cycle

[7]–[9], and the rectangular QV cycle [10]. The work in [11] presents a detailed qualitative comparison between the convertible energy available to each configuration.

Building on the electrical analysis of the circuit presented in Part 1, in this work, we will present the full coupled electromechanical system and its analysis. In the electrical analysis we normally assume that the maxima and minima of C_t are known, C_{max} and C_{min} respectively. In reality C_{max} and C_{min} are defined by the amplitude of the resonator displacement which is not known *a priori*. Indeed, the resonator displacement depends on the external mechanical force, structure of the resonator and the electrical force of the transducer, generated by the conditioning circuit. To have a full picture of the coupled electrical and mechanical domains, the system in both domains should be considered in some unified analysis. Very few works have addressed the coupling between the electrical and mechanical forces in eKEHs [12] and to the authors' best knowledge, no such analysis has been undertaken for conditioning circuits implementing a rectangular QV cycle (e.g., the Bennet's doubler [13]).

This study is applied to any conditioning circuit implementing a rectangular QV cycle. The generality of this study can be explained as follows: for a fixed rectangular cycle and given transducer configuration $C_t(x)$, the transducer force is fixed $F_t = f(C_t(x), V)$. Therefore the electromechanical energy conversion and mechanical behavior is not sensitive to the particular architecture of conditioning circuit as far as the rectangular QV cycle is implemented.

In this study we have chosen the charge pump with resistive flyback [14] for three reasons: i) it implements a rectangular QV cycle, ii) by accurately choosing the resistive load this configuration can model the behavior of the charge pump with inductive flyback [10], [15], [16] or of the Bennet's doubler, and iii) it is suitable for analytical analysis. Therefore, while this article is presented in terms of the charge pump conditioning circuit, the analysis is universal to all conditioning circuits implementing the rectangular QV cycle.

Analytical and semi-analytical methods not only provide validation of the numerical simulations but also provide a greater understanding of the system dynamics, and where numerical simulations are generally long computer intensive operations, analytical and semi-analytical models allow faster solutions of the system and the possibility of multi-parameter analysis.

We examine the nonlinear behavior in the system and develop an analytical event driven model to aid numerical results. The system is examined using the Multiple Scales Method

(MSM) perturbation technique, treating the eKEH as a nonlinear oscillator with a nonlinear transducer force. The application of perturbation techniques allows us to determine the transient and steady-state dynamics for multi-parameter simulations and gives a greater understanding of the system operation.

The original measurements used for the validation of this study were done with the experimental set-up presented in [16]. This work implemented, for the first time, a charge pump with inductive flyback employing a fabricated MEMS device. The used MEMS device was characterized in [5].

In this paper the layout is as follows. In Section II the three coupled mechanical models are presented. The Multiple Scales Method analysis is presented in Section III along with steady-state oscillations. The nonlinear dynamics which exist in circuits of this type are presented in Section IV. Section V presents a novel method for calculating the frequency shift occurring as a result of the nonlinear coupling. Finally, in Section VI, the results are compared with experimental results from the fabricated device.

II. STATEMENT OF THE PROBLEM

In this work we employ three models to describe the system; a behavioral model of the circuit implemented in the VHDL-AMS/SPICE environment, a set of differential equations derived from Newton's second law and Kirchhoff's circuit equations, and a simplified model that was the basis for semi-analytic results. Consistency between the models was ensured at each stage of the work by comparing the solutions of the differential equations and simplified model with the VHDL results.

A. VHDL-AMS/Spice Behavioral Model

The model of the system was achieved using a mixed behavioral description implemented in the VHDL-AMS/SPICE environment provided with the AdvanceMS tool of Mentor Graphics. The model is realized as follows. The conditioning circuit is described as an electrical network described by an Eldo netlist, where Eldo is a commercial variant of SPICE. The transducer and resonator block is implemented by a VHDL-AMS model, seen as an electrical dipole behaving as a variable capacitor [17].

B. Numerical Model

A simple electrostatic harvester consists of a high quality resonator, a variable capacitor (transducer) C_t, and a conditioning circuit (Fig. 1). Thus as the displacement, x, of the mobile mass is affected by both the external vibrations and the transducer force f_t, it can be described by the following Newtonian equation

$$\ddot{x} + (b/m)\dot{x} + \omega_0^2 x = A_{ext}\cos(\omega_{ext}t) + f_t/m \quad (1)$$

where m is the mass of the resonator, b is the damping factor, $\omega_0 = \sqrt{k/m}$ is the natural frequency, k is the spring constant, A_{ext} is the acceleration amplitude of external vibrations and ω_{ext} is the frequency of the external vibrations. The overdot denotes the derivative with respect to time, t. Note that the initial conditions for the displacement and velocity can be any, and we can assume them to be zero $x(0) = \dot{x}(0) = 0$. The initial conditions for all voltages are the same: $V_{res}(0) = V_t(0) =$
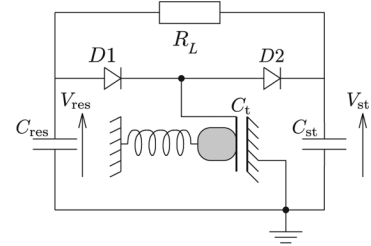

Fig. 1. Electrostatic kinetic energy harvester employing a charge pump conditioning circuit with resistive flyback. This harvested energy facilitates the pumping of charges from the large reservoir capacitor, C_{res}, to the smaller storage capacitance, C_{st}, where $C_{res} \gg C_{st} \gg C_t$.

$V_{st}(0) = V_0$. The transducer force f_t is dependent on x (the mobile mass position) and V_t (the transducer voltage)

$$f_t(x, V_t) = \frac{V_t^2}{2}\frac{dC_t}{dx} \quad (2)$$

Making use of diode models, capacitor models and applying Kirchhoff's circuit laws the system can be reduced to a further three differential equations describing the voltages; V_{res}, V_t, V_{st}

$$\dot{V}_{st} = \frac{1}{C_{st}}\left(K(-V_t - V_{st}) - \frac{(V_{st} - V_{res})}{R}\right) \quad (3)$$

$$\dot{V}_{res} = \frac{1}{C_{res}}\left(\frac{(V_{st} - V_{res})}{R} - K(V_{res} + V_t)\right) \quad (4)$$

$$\dot{V}_t = \frac{1}{C_t}\left((K(-V_t - V_{st}) - K(V_{res} + V_t))\right.$$
$$\left. - V_t\dot{x}\frac{dC_t}{dx}\right) \quad (5)$$

where K is the diode model current $K(V) = I_s(e^{qV/kT} - 1)$ [18].

In this paper we consider the symmetrical gap closing transducer [5], denoted SGC throughout this paper for variables that are directly changeable with the choice of transducer configuration. This defines the form of the variable capacitance, C_t, and its derivative, dC_t/dx. They are described by:

$$C_t = \frac{2C_0}{1 - (x/d)^2}, \quad \frac{dC_t}{dx} = \frac{4C_0 d^2 x}{(d^2 - x^2)^2} \quad (6)$$

where $C_0 = \epsilon_0 S/d$ and ϵ_0 is the permittivity of a vacuum. To reduce the number of parameters in the system and outline only essential ones, the system was normalized

$$y'' + 2\beta y' + y = \alpha\cos(\Omega\tau) + f_t(y, y', U_t) \quad (7)$$

$$U'_{st} = \phi_1 F(-U_t - U_{st}) - \frac{(U_{st} - U_{res})}{\tau_1} \quad (8)$$

$$U'_{res} = \frac{(U_{st} - U_{res})}{\tau_2} - \phi_2 F(U_{res} + U_t) \quad (9)$$

$$U'_t = \phi_3 \mathcal{C}(y)\left(F(-U_t - U_{st}) - F(U_{res} + U_t)\right)$$
$$- \mathcal{V}(U_t, y, y') \quad (10)$$

where $y = x/d$, $U_{t,st,res} = V_{t,st,res}/V_0$, $\tau = \omega_0 t$, $\Omega = \omega_{ext}/\omega_0$, $\beta = b/2m\omega_0$, $\alpha = A_{ext}/d\omega_0^2$, $\phi_1 = I_0/\omega_0 V_0 C_{st}$, $\tau_1 = C_{st}\omega_0 R_L$, $\phi_2 = I_0/\omega_0 V_0 C_{res}$, $\tau_2 = C_{res}\omega_0 R_L$, $\phi_3 = I_0/2\omega_0 V_0 C_0$, and F is the dimensionless diode model $F(U) = (e^{qV_0 U/kT} - 1)$. The prime denotes the derivative with respect to dimensionless time τ. The form of the functions $\mathcal{C}(y)$, $\mathcal{V}(U_t, y, y')$ and $f_t(y, y', U_t)$ depend on the transducer

Proof mass (m)	$66 \cdot 10^{-6}$ kg
Initial gap between fingers (d_0)	$43.5 \cdot 10^{-6}$ m
No. of fingers (N)	142
Length of fingers (l)	$1.97 \cdot 10^{-3}$ m
Finger thickness (h)	$380 \cdot 10^{-6}$ m
Location of Stoppers	$36 \cdot 10^{-6}$ m
Damping Factor (b)	$7.9 \cdot 10^{-3}$ Nsm^{-1}
Quality factor (Q)	8.5
Spring constant (k)	68 Nm^{-1}
Aspect ratio of sidewalls (α_r)	0.013
Diode Threshold Voltage	0.35V
S	$1.063 \cdot 10^{-4}$ m^2
C_{st}	$3.3 \cdot 10^{-9}$ F
C_{res}	$1.0 \cdot 10^{-6}$ F
A_{ext}	$0.3g$

geometry. To present the normalized system of (7)–(10) in a more general manner, and highlight the transducer dependent terms, we present the transducer dependent functions separately. For the symmetrical gap closing transducer, the terms $\mathcal{C}(y)$, $\mathcal{V}(U_t, y, y')$, and $f_t(y, y', U_t)$ are:

$$\mathcal{C} = (1 - y^2), \quad \mathcal{V} = \frac{2U_t y' y}{1 - y^2}, \quad f_t = \psi_{SGC} \frac{U_t^2 y}{(1 - y^2)^2} \quad (11)$$

where $\psi_{SGC} = 2C_0 V_0^2 / m\omega_0^2 d^2$.

C. Simplified Model

The acceleration amplitude of external vibrations, A_{ext}, the initial voltage on the capacitors, V_0, and the load resistance, R_L, may vary and affect the behavior of the system. We refer to them as the control parameters of the dynamical system. The experimental parameters used in this study are listed in Table I.

The simplified model is obtained by reducing the system of differential equations to one differential (7) with a piecewise defined transducer force f_t. In order to do this, we take three assumptions:

- U_{res} can be assumed constant.
- U_{st} is constant after the transient process.
- Diodes are ideal with a threshold voltage $U_{D\,on}$.

Such a circuit implements, exactly, the rectangular QV cycle presented in Section II of the Part 1 article.

The first assumption is valid since by the circuit design, C_{res} is very large such that the voltage variation across it is indeed negligible.

Since C_{st} is significantly larger than C_{max}, the variation of the voltage across it is negligible compared to U_t. Therefore, $U'_{st} = 0$, however the value of U_{st} after the transient process is not known and can be determined by assuming that, after a sufficient transient has passed, C_{st} has saturated and so draws no further current (cf. Section III-B Part 1). Thus equating the average change in charge on C_t to the average current flowing through the load (R_L), in one cycle, we obtain the following equation:

$$U_{st} = V_0 \left(\frac{\frac{T_0}{R_L} + C_{max}}{\frac{T_0}{R_L} + C_{min}} \right) \quad (12)$$

where T_0 is the period of driven oscillations and C_{max} and C_{min} are the maximum and minimum values of C_t during one cycle of oscillations. Note C_{max} and C_{min} are functions of the resonator displacement (x), as shown in (6), which is a dynamical quantity.
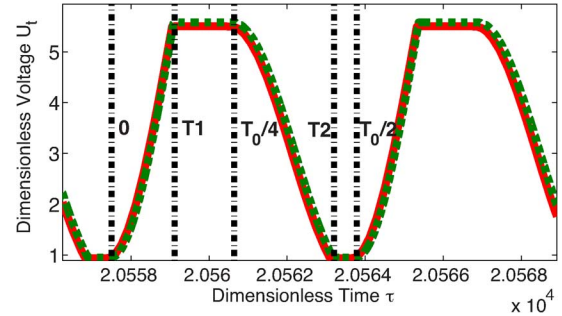

Fig. 2. A generic comparison of the dimensionless U_t obtained from numerical simulations (red line) and the solution of the improved simplified model (dotted green line) employing (13). The figure describes the events during one half cycle of oscillations in the resonator: $0 \leq \tau < T_1$ both diodes are off (stage 1), $T_1 \leq \tau < T_0/4$ the second diode is on (stage 2), $T_0/2 \leq \tau < T_2$ both diodes are off again (stage 3) and $T_2 \leq \tau < T_0/2$ the first diode is on (stage 4).
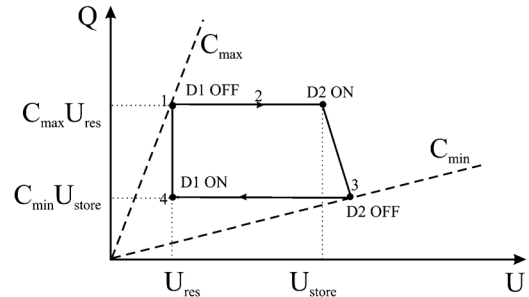

Fig. 3. QV cycle over one oscillation cycle for the charge pump circuit with resistive flyback. The area enclosed in one cycle is equal to the energy harvested during that cycle.

The approximation (12), presented in [19], was improved significantly by including the threshold diode voltages. The resulting approximation is shown in Fig. 2. The inclusion of the threshold voltages resulted in the following equation:

$$U_{st} = V_0 \left(\frac{\frac{T_0}{R_L} + C_{max}}{\frac{T_0}{R_L} + C_{min}} - U_{D\,on} \frac{C_{max} + C_{min}}{\frac{T_0}{R_L} + C_{min}} \right) \quad (13)$$

where $U_{D\,on}$ is the dimensionless diode threshold voltage.

The variable voltage across the transducer U_t can be found by analyzing one cycle of the resonator oscillations and sequencing the stages of circuit operation. U_t is approximated as an event driven oscillation developed as a function of the capacitance. From Fig. 3 one can see the change of state in U_t at both C_{max} and C_{min}, from D1 on to D1 off and from D2 on to D2 off respectively. We model U_t over one full cycle of steady-state oscillations. While the model presented in [19] was a four piece function, the configuration of the SGC transducer doubles the frequency of C_t, and therefore U_t, oscillations. Therefore our model of U_t is an eight part function.

However, to simplify our explanation we will discuss the first four terms which are simply repeated for the eight part piecewise function. Fig. 2 presents a four part approximation, detailed below, against the corresponding numerical simulation.

Estimating the maxima and minima of U_t as constants, simply equal to $U_{st} + U_{D2on}$ and $U_{res} - U_{D1on}$ the four part approximation requires two further U_t and τ expressions. We achieve this by finding the analytical solution of U_t for both diodes off and using it to calculate the times at which it reaches the magnitude of the U_t maximum (T_1) or minimum (T_2). When both diodes are off, (10) simplifies to:

$$U'_t = \mathcal{V}(U_t, y, y') \quad (14)$$

The analytical solution can easily be determined by subbing $y = a\cos(\tau + \varphi)$ into (14), where $y = a\cos(\tau + \varphi)$ is the first approximation for the displacement (see the Multiple Scales Method in the next section), and solving for U_t:

$$U_t = const \cdot \left(a^2 \left(-\cos(2\Omega\tau) \right) - a^2 + 2 \right) \quad (15)$$

where $const$ is a constant of integration. The expressions in (15) describe the behavior of U_t in two regions, $0 < \tau < T_1$ and $T_0/4 < \tau < T_2$.

Stage 1 starts at the moment when the capacitance of the transducer is maximal, i.e., $C_t = C_{max}$. We denote this moment of time as $\tau = 0$, and both diodes are turned off. From Fig. 3 we can see that, for this scenario, diode 1 has just turned off. Thus our initial condition for U_t is $U_t(0) = U_{res} - U_{D1on}$ and we can therefore calculate $const$ from (15). The resulting expression is $v_1(a, \tau)$ in (19).

Stage 2 starts at time $\tau = T_1$. This event occurs when the voltage U_t reaches the value that is required to turn on diode 2, i.e., D1 off, D2 on. As we approximate the diodes as an ideal diode with dimensionless threshold voltage $U_{D\,on}$, $U_t(T_1) = U_{st} + U_{D2on}$. Therefore we realize the following equation which allows us to calculate T_1:

$$v_1(a, T_1) = U_{st} + U_{D2on} \quad (16)$$

Note that T_1 is a function of $tv_1(a)$ which is presented in (19).

Stage 3 begins when the capacitance of the variable transducer reaches its minimal value C_{min}. The corresponding moment in time is $\tau = T_0/4$. As diode 2 has just turned off, the initial condition for U_t is $U_t(T_0/4) = U_{st} + U_{D2on}$. As in *Stage 1* this allows us to evaluate $const$, from (15), where $v_2(a, \tau)$ (in (19)) is the corresponding U_t expression.

Finally, *Stage 4* commences at $\tau = T_2$, which is the moment at which the voltage across the transducer reaches the value required to turn on diode 1:

$$U_t(T_2) = U_{res} - U_{D1on} \quad (17)$$

Thus, as in *Stage 2*, the time T_2 can be calculated by letting the two knowns equal each other:

$$v_2(a, T_2) = U_{res} - U_{D1on} \quad (18)$$

Stage 4 lasts until C_t reaches its maximal value at $\tau = T_0/2$. From this point, the piecewise approximation continues with T_3 and T_4 found in a similar fashion with the difference being that they are shifted by $T_0/2$. After the eight part solution, the new cycle of oscillation begins. The analytical terms of the U_t function are given below:

$$SGC = \begin{cases} v_1(a, \tau) = \left(2 - a^2 - a^2\cos(2\Omega\tau)\right)\left(\dfrac{U_{res} - U_{D1on}}{2 - 2a^2}\right) \\ v_2(a, \tau) = \left(2 - a^2 - a^2\cos(2\Omega\tau)\right)\left(\dfrac{U_{st} + U_{D2on}}{2}\right) \\ tv_1(a) = \left(\dfrac{-1}{a^2}\left(a^2 - 2 + (2 - 2a^2)\dfrac{(U_{st} + U_{D2on})}{U_{res} - U_{D1on}}\right)\right) \\ tv_2(a) = \left(\dfrac{-1}{a^2}\left(a^2 - 2 + 2\dfrac{(U_{res} - U_{D1on})}{U_{st} + U_{D2on}}\right)\right) \end{cases} \quad (19)$$

where $v_1(a, \tau)$ and $v_2(a, \tau)$ are two functions in the eight part piecewise U_t approximation and $tv_1(a)$ and $tv_2(a)$ represent two of the switching times. Combining all parts of the piecewise approach, we describe the voltage U_t with good accuracy as shown in Fig. 2. Inserting the piecewise description of U_t

into f_t, in (11), allows a piecewise description of the transducer force, presented in (21). Thus, the simplified model of the system is given by the equation:

$$y'' + 2\beta y' + y = \alpha\cos(\Omega\tau) + f_t(y, U_t) \quad (20)$$

$$\frac{f_t}{\psi_{SGC}} = \begin{cases} v_1(y_{max}, \tau)^2 \dfrac{y}{(1 - y^2)^2}, & 0 < \tau < T_1 \\ \left(U_{st}(y_{max}) + U_{D2on}\right)^2 \dfrac{y}{(1 - y^2)^2}, & T_1 < \tau < T_0/4 \\ v_2(y_{max}, \tau)^2 \dfrac{y}{(1 - y^2)^2}, & T_0/4 < \tau < T_2 \\ \left(U_{res} - U_{D1on}\right)^2 \dfrac{y}{(1 - y^2)^2}, & T_2 < \tau < T_0/2 \\ v_1(y_{max}, \tau)^2 \dfrac{y}{(1 - y^2)^2}, & T_0/2 < \tau < T_3 \\ \left(U_{st}(y_{max}) + U_{D2on}\right)^2 \dfrac{y}{(1 - y^2)^2}, & T_3 < \tau < 3T_0/4 \\ v_2(y_{max}, \tau)^2 \dfrac{y}{(1 - y^2)^2}, & 3T_0/4 < \tau < T_4 \\ \left(U_{res} - U_{D1on}\right)^2 \dfrac{y}{(1 - y^2)^2}, & T_4 < \tau < T_0. \end{cases} \quad (21)$$

where the dimensionless transducer force f_t is scaled by ψ_{SGC} as described in (11) and the event driven time limits in (21) are:

$$\begin{aligned} T_1(a) &= \frac{1}{2\Omega}\arccos\left(tv_1(a)\right), & T_0/4 &= \frac{\pi}{2\Omega} \\ T_2(a) &= \frac{\pi}{\Omega} - \frac{1}{2\Omega}\arccos\left(tv_2(a)\right), & T_0/2 &= \frac{\pi}{\Omega} \\ T_3(a) &= T_1(a) + \frac{\pi}{\Omega}, & 3T_0/4 &= \frac{3\pi}{2\Omega} \\ T_4(a) &= T_2(a) + \frac{\pi}{\Omega}, & T_0 &= \frac{2\pi}{\Omega} \end{aligned} \quad (22)$$

This reduces the system of differential equations to one differential equation, (7), with a piecewise force f_t. Solving the system of differential equations, above, is long and computer intensive thus this approximation is very useful for numerical solutions also as it greatly reduces the complexity. We can also use this model to apply the multiple scales method in a similar fashion as that described in [9].

III. MULTIPLE SCALES METHOD AND STEADY-STATE OSCILLATIONS

The method of multiple scales (MSM) is an asymptotic method that is often applied for the analysis of weakly non-linear oscillators [20], both autonomous and under external excitation.

The form of the method studied in this work, applied to the constant charge eKEH conditioning circuit, is derived in full in [9]. Only terms important to our study are included in this article. It is applicable to all eKEHs, as long as the dimensionless parameters β, α, ψ and σ in (7) are comparatively small relative to unity, where $\sigma = \Omega - 1$ is the frequency mismatch between the external driving frequency and the natural resonance frequency of the resonator. Typical values of the dimensionless parameters for the real experimental data with (an external vibration amplitude, $A_{ext} = 0.3$ g, and a nominal initial voltage, V_0, of 20 V) give $\alpha = 0.0586$, $\beta = 0.0587$ and $\psi = 0.0968$, which are clearly small terms.

A requirement of the presented method is that the transducer force f_t be periodic. It is also advantageous that the system be high Q, which is the case for narrow band energy harvesters and so is fulfilled. Please note, however, that this method can incorporate higher Fourier coefficients and also allows for the inclusion of mechanical nonlinearities as presented in [21].

The multiple scales method approaches the eKEH as a simple resonator with a perturbation term. It then solves this by introducing different time scales.

As the transducer force f_t is periodic with period T it can be described as a Fourier series and as this is a narrow band energy harvester the first harmonic of the Fourier series should be sufficient in approximating f_t:

$$f_t(y_0, U_{t,0}) = f_0(a) + a_1(a)\cos(T_0 + \phi) + b_1(a)\sin(T_0 + \phi) \tag{23}$$

The Fourier coefficients for the symmetrical gap closing transducer are:

$$f_0(a) = \frac{\Omega}{2\pi}\int_0^T f_t(y_0, U_{t,0})dt$$

$$a_1(a) = \frac{\Omega}{\pi}\int_0^T f_t(y_0, U_{t,0})\cos(\Omega t)dt$$

$$b_1(a) = \frac{\Omega}{\pi}\int_0^T f_t(y_0, U_{t,0})\sin(\Omega t)dt \tag{24}$$

The total solution of y can be described by

$$y(\tau) = a\cos(\tau + \psi) \tag{25}$$

where $\psi = \sigma T_1 - \phi$. Obtained by the same method as in [9], the equations providing information about the transient dynamics of the system are presented in (26). They describe the slow amplitude a and phase ψ of the mobile mass oscillations in the transient and steady-state modes:

$$\dot{a} = -\beta a - \frac{b_1(a)}{2} + \frac{\alpha}{2}\sin(\psi)$$

$$a\dot{\psi} = a\sigma + \frac{a_1(a)}{2} + \frac{\alpha}{2}\cos(\psi) \tag{26}$$

By setting $\dot{a} = 0$ and $\dot{\psi} = 0$ and taking a phase $\dot{\psi}_0$ we can combine the steady-state solutions into one equation. The resulting equation provides a solution for the steady-state amplitude of oscillations, a_0:

$$\frac{\alpha^2}{4} = \left(a_0\sigma + \frac{a_1(a_0)}{2}\right)^2 + \left(\beta a_0 + \frac{b_1(a_0)}{2}\right)^2 \tag{27}$$

In conjunction with (25), we obtain the steady-state solution of y of the form

$$y_0(\tau) = a_0\cos\left((1+\sigma)\tau - \psi_0\right) \tag{28}$$

where a_0 and ψ_0 are the steady-state amplitude and phase of oscillations. The index "0" is used to emphasize that this is a steady-state solution. Formally, $x_0 = (a_0, \psi_0)$ is a fixed point of the set (26). Some transducer geometries experience a constant shift in the oscillations (described by y_{av} in [9]). However, due to the symmetry of the SGC device in this study, there is no average displacement.

According to the Routh-Hurwitz criterion, the point (a_0, ψ_0) is stable if the conditions in (29) are met. However, this stability condition is necessary, but not entirely sufficient.

$$2\beta + \frac{b_1'}{2} + \frac{b_1}{2a_0} > 0$$

$$\left(\beta + \frac{b_1'}{2}\right)\left(\beta + \frac{b_1}{2a_0}\right) + \left(\sigma + \frac{a_1'}{2}\right)\left(\sigma + \frac{a_1}{2a_0}\right) > 0 \tag{29}$$
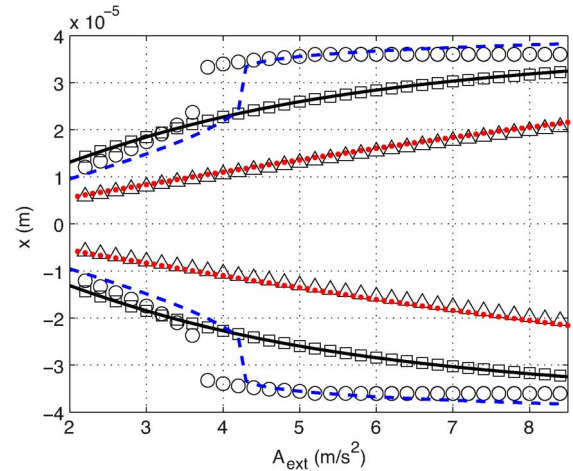

Fig. 4. The envelope of oscillations for a sweep of external vibration amplitude A_{ext} comparing the numerical and MSM solutions, for different values of the small parameter σ. The numerical solution at $\omega_{ext} = 160$ Hz (i.e., $\sigma \approx 0$) is shown by the squares. The MSM solution (full black line) clearly agrees very well in this case. The other two cases represent the same simulation with a difference of $\sigma \approx \pm 0.125$. The solutions for $\omega_{ext} = 140$ Hz are shown by circles (numerical) and the dashed blue line (MSM). The triangles (numerical) and dotted red line (MSM) describe the envelope of oscillations for $\omega_{ext} = 180$ Hz.

If the conditions, in (29) are not satisfied, the orbit defined by a_0 and ψ_0 is unstable (a saddle orbit). The importance of this stability will be presented later. The derivation of (29) is presented in [9].

Envelopes of oscillations for varying external vibration amplitudes and three different values of σ (normalized frequency mismatch between external vibrations and the natural frequency) are presented in Fig. 4. They compare the solution of the numerical differential equations with the MSM solution. Solutions of the differential equations were in very close agreement with VHDL/Spice simulations and so can, essentially, be considered equivalent.

Fig. 4 presents two example cases for $\sigma \approx \pm 0.125$ compared with the scenario when $\sigma \approx 0$. Based on the figure, we verify the accuracy of the simplified model with MSM to have good accuracy with the numerical models of the system, even for an increase in the magnitude of σ. Results of the semi-analytic model are presented in later sections.

IV. BIFURCATION AND COMPLEX BEHAVIOR

For nonlinear oscillators it is established that an increase in system parameters or in the amplitude of the external force results in bifurcations of previously stable orbits and, ultimately, to irregular, chaotic behavior [22].

Without the transducer force, the system described by (1) is simply a driven oscillator. We can solve this analytically and thus understand the dynamics, amplitude of vibrations, etc., and so determine the maximum harvested energies. The nonlinear force f_t describes the interaction of the mechanical and electrical domains and its presence in (1) results in there being no closed form solution. The effect of this nonlinearity is essentially the focus of this paper as it is the electromechanical coupling. This is what makes this study universal to all circuits which implement a rectangular QV cycle as the force "seen" by the mechanical resonator is equivalent for all similar QV cycles.

Fig. 5 presents a bifurcation diagram depicting the change of dynamics in the resonator displacement as the amplitude of
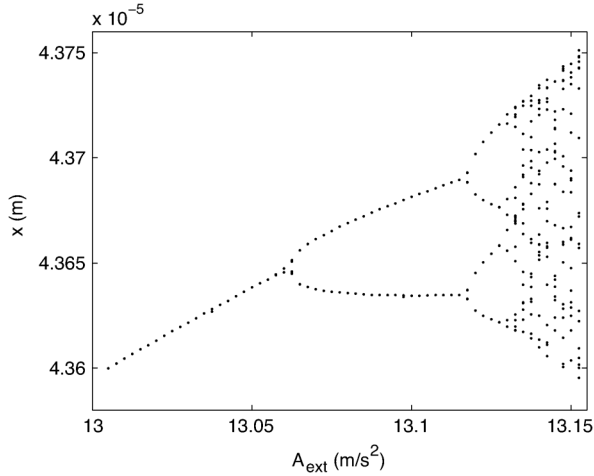
Fig. 5. A bifurcation diagram, taken using a Poincaré section, showing the changing dynamics in the resonator for a sweep of potential external vibrations (A_{ext}). Note the scale of the oscillations: the stoppers were moved to allow this study of the nonlinear dynamics.

external vibrations (A_{ext}) is varied. Note that there are no mechanical nonlinearities included in this analysis and yet we find that the nonlinear damping force f_t results in a period doubling cascade before reaching chaotic behavior. The nonlinear effect of the non-conservative force (f_t) is another example of the complex behavior which results from the electromechanical coupling in eKEHs.

We can characterize and analyze the change in dynamics presented in Fig. 5 in many ways. In this study we have calculated Floquet multipliers and checked Lyapunov stability in the form of Lyapunov exponents.

Due to spacial constraints we only briefly discuss some of the techniques used in this study to understand the system dynamics. The Floquet multipliers provide an insight into the stability of the orbit. The orbit is asymptotically stable if there are no eigenvalues outside the unit circle. If, for some change in control parameter, a Floquet multiplier leaves the unit circle it signifies that a bifurcation has occurred. Depending on the point at which the multiplier exits the unit circle, the bifurcation can be characterized. For the parameters presented in Fig. 5, a Floquet multiplier leaves the unit circle through -1 at approximately 13.06 m/s^2. Therefore, not only does this highlight the existence of a bifurcation point around 13.06 m/s^2, it also indicates that the original orbit undergoes a doubling bifurcation. Lyapunov exponents are the real parts of the Floquet multipliers. The Lyapunov exponents or characteristic exponents are associated with a trajectory and essentially measure the average rates of expansion and contraction of trajectories surrounding it [22]. The largest Lyapunov exponent provides a good understanding of the systems transition to chaos. Formal mathematical definition of the largest Lyapunov exponent can be explained in the following way. Take $x_0(t)$ to be a steady state trajectory or a fixed point in the state space. If at $t = 0$ a perturbed trajectory, $x(t)$, is initiated, locally, and allowed to run until a time t, the resulting largest Lyapunov exponent is described by the expression:

$$\lambda_1 = \lim_{t \to \infty} \frac{1}{t} \log \frac{\|x(t) - x_0(t)\|}{\|x(0) - x_0(0)\|} \tag{30}$$

where x_0 represents the original set of nonlinear equations and x is the system x_0 with the inclusion of a small perturbation to

its initial conditions. For a change in control parameters, if λ_1 becomes positive the system has entered a chaotic regime.

To extract a more comprehensive understanding of the system dynamics, Lyapunov exponents corresponding to each system variable can be calculated. This is formulated in a similar manner as the largest exponent with the difference being that each exponent is analyzed separately. To achieve this, each perturbation has to be orthogonal. This can be implemented using the Gram-Schmidt process [22]. The largest Lyapunov exponent does not need orthogonality as for each solution it will simply calculate the largest Lyapunov exponent on the most unstable plane. The benefit of calculating the separate Lyapunov exponents is that we can see the individual evolutions.

From the Lyapunov analysis, we see that one of the exponents is zero close to $A_{ext} = 13.06$ m/s^2. This signifies a bifurcation has occurred and is in agreement with the first bifurcation point in Fig. 5. The exponents become negative again before becoming zero at approximately $A_{ext} = 13.12$ m/s^2, corresponding to the second bifurcation point. The exponents become positive at approximately $A_{ext} = 13.13$ m/s^2 signifying chaotic behavior confirming the dynamics shown in Fig. 5.

V. MODIFICATION OF RESONANT FREQUENCY DUE TO ELECTROMECHANICAL COUPLING

In the application of narrow band energy harvesters, for which most eKEHs are designed, operating the system around the resonant frequency is very important to maximise the energy available for harvesting.

As discussed above in Section IV, the coupling between the mechanical and electrical domains has a significant impact on the resonator dynamics in the system. The transducer force f_t alters the effective spring stiffness of the system and therefore changes the resonant frequency of the system.

If the force is conservative (only dependent on the displacement) it can be assimilated as a nonlinear spring, whose stiffness is the full derivative of the transducer force:

$$-k_t x = \left(\frac{df_t}{dx} \right) x \tag{31}$$

The term k_t influences the resonant frequency according to the simple equation:

$$\omega_{res} = \sqrt{\frac{k + k_t}{m}} \tag{32}$$

Clearly, in the case when k_t is positive it will result in electrostatic hardening and in the case of a negative k_t the resonant frequency is lowered, softening the response. Any type of transducer can easily be accommodated in this formula.

In the case of capacitive energy harvesters the force depends both on the velocity and the displacement. Thus the actual modification of the frequency can only be determined by a full analysis of the coupled system.

In the rectangular QV cycle conditioning circuit, the force can be assumed conservative only in two extreme cases: i) for the case when $V_{res} = V_{st}$ and ii) when the charge pump has saturated (cf. saturation discussion in Part 1). In the first case i) the bias voltage on the capacitor is fixed equal to V_{res} such that the force is:

$$f_t(x) = \frac{V_{res}^2}{2} \frac{dC_t}{dx} \tag{33}$$

and for the second case ii) the charge on the capacitor is fixed equal to $Q = C_{max}V_{res}$, giving the transducer force:

$$f_t(x) = \frac{Q^2}{2C_t^2}\frac{dC_t}{dx} \qquad (34)$$

Combining (31) and (32), it can be proven that the resonance frequency shift for the two configurations presented in (33) and (34) represent the limits of the shift in the resonance frequency, for a given transducer.

The frequency shift for any nontrivial rectangular QV cycle, for any transducer, will be inside the limits given by (32). For the three most common transducer geometries, area overlap (AO), simple gap closing (GC) and symmetrical gap closing transducer (SGC) the pair of extreme k_t values are presented in Table II. This provides further verification of the novel approach to determine the frequency shift presented below.

We now present our novel method for calculating the frequency shift due to the electromechanical force f_t for any QV cycle. To the best knowledge of the authors, a tool to determine the magnitude of the potential electrostatic shift in oscillations of eKEH devices has not previously been presented.

The method is a simple application of the multiple scales method which allows the user calculate the resonant frequency shift caused by electrostatic softening.

Equation (27) is an implicit function of both a_0 and σ. Denoting (27) as $H(a_0, \sigma)$ and taking the partial derivatives $H'_{a_0}(a_0, \sigma)$ and $H'_\sigma(a_0, \sigma)$ we can determine the implicit derivative:

$$\frac{da}{d\sigma} = \frac{\left(a_0\sigma + \frac{a_1(a_0)}{2}\right)a_0}{2a_0\beta^2 + \beta b_1(a_0) + \beta a_0\frac{\partial b_1(a_0)}{\partial a_0} + \frac{b_1(a_0)}{2}\frac{\partial b_1(a_0)}{\partial a_0}} \qquad (35)$$

Setting this equal to 0 to find its extremum, the resulting formula for the frequency shift is:

$$\sigma = -\frac{a_1(a_0)}{2a_0} \qquad (36)$$

This result highlights the dependence of the frequency shift on the first Fourier cosine term of the transducer force, and as this term is nonzero we will have a frequency shift for different parameters. Interestingly, for the constant charge conditioning circuit presented in [9], the formula is correct as $a_1(a_0) = 0$ and there is no frequency shift in the oscillations.

Even in cases when σ is large and the multiple scales method is no longer as accurate this tool is still very useful, at least to give an impression of the scale of the resonance shift and so limit the range of numerical simulations.

Fig. 6 compares the numerical frequency shift with the solution of (36) for the experimental symmetrical gap closing device. Also included in the plot are comparisons of the frequency shift for both a simple gap closing and area overlap transducer, given as

$$C_{t,GC} = \frac{C_0}{1 - (x/d)}, \quad C_{t,AO} = C_0 + \alpha_{t,AO}x \qquad (37)$$

respectively. The parameters from Table I were used for all transducers with the exception that the area of the capacitor plates was altered (and the gap between plates itself for the gap closing transducer) to give equal C_{max} and C_{min} values, at the maximum displacement allowed by the geometry (cf Section VI-B). We have previously presented the multiple scales analysis of these transducers in [19].

TABLE II
EXTREME k_t LIMITS

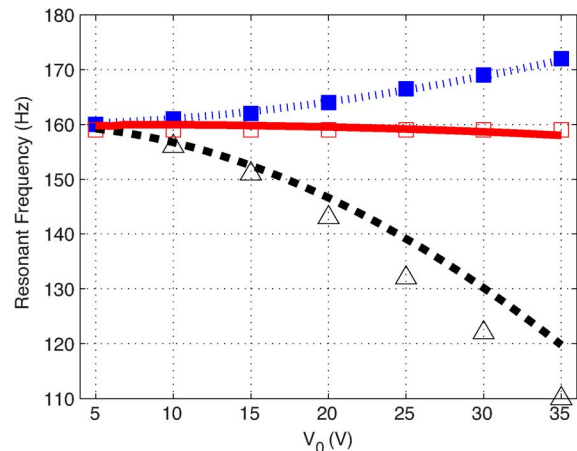| Transducer	k_t for Fixed V	k_t for Fixed Q
AO	0	$\frac{\alpha_{t,AO}^2 Q_0^2}{C_0^3}$
GC	$-V_{res}^2\frac{C_0}{d^2}$	0
SGC	$-2V_{res}^2\frac{C_0}{d^2}$	0

Fig. 6. A comparison of the resonant frequencies at different initial biasing voltages for the three most common transducer configurations. The numerical symmetrical gap closing transducer solution is represented by the black triangles and the corresponding solution of (36) shown by the black dot/dash line. The filled blue squares describe the numerical area overlap transducer, in comparison with the AO solution of (36) plotted as the dotted blue line. The simple gap closing transducer is the middle waveform, shown by the red squares (numerical) and the solid red line (solution of (36)).

In Fig. 6 we see large electrostatic softening in the case of the symmetrical gap closing transducer (hysteresis is present at $V_0 = 25$ V and higher voltages), a minimal change for the simple gap closing transducer and a small increase in the resonant frequency of the area overlap transducer. The frequency shift is clearly a function of the transducer geometry, but it is also dependent on the QV cycle and parameters of the system. For different transducer parameters the simple gap closing transducer also experiences a modification of the resonance frequency.

Experimental confirmation of our analysis describing the resonant frequency shift due to electromechanical coupling is presented in Section VI.

VI. EXPERIMENTAL VERIFICATION OF MODEL

A. Experimental Set-Up

The experimental set-up which we use to validate our analysis was presented in [16]. It consists of a charge pump with inductive flyback [10]. The inductive flyback was actuated by a fixed periodic time sequence (cf. detailed description in Part 1). The used MEMS device is a micro resonator coupled with a capacitive transducer, submitted to sinusoidal external vibrations with fixed frequency and amplitude. The MEMS device was characterized in [5] and these parameters are provided in Table I.

B. Transducer Model

The transducer described in [5] experiences an undercut due to the etching, by deep reactive ion etching (DRIE). This results

in a more complicated model for the capacitance, including logarithmic functions.

To employ our analysis we introduced a simple equivalent model of a symmetrical gap closing transducer, as shown in (6). To accommodate the undercut by DRIE for our simplified model we took the average gap between the fixed and movable fingers to be:

$$d = d_0 + h\alpha_r,$$

where h is the height of the silicon substrate and defined in the orthogonal direction to the substrate plane, α_r is the ratio of the silicon undercut by DRIE and d_0 is the gap between the fixed and movable fingers at the top of the comb.

In an equivalent manner to the fitting of the theoretical values and experimental results described in [5] we calculated the maxima and minima of the capacitance, C_t, allowed by the geometry. The net experimental values (88 pF/40 pF) compare very well with our theoretical values of (86.8 pF/38.8 pF).

C. Description of Experiment and Model Equivalence

In the experimental setup, it is not possible to measure the displacement of the MEMS resonator. This makes validation of the analytical model difficult. However, based on our analytical model, we can compute and derive quantities that can easily be measured, and that are related to the dynamics of the resonator.

The implemented experiment measured the steady-state value of the voltage V_{st} (denoted $V_{st\ ss}$), when the charge pump operated *without flyback* starting from the initial voltage on C_{st} capacitor:

$$V_{st0} = V_{res}, \tag{38}$$

where V_{res} is a controlled (input) parameter of the experiment. Such a model is equivalent to the architecture in Fig. 1, with $R_L = \infty$.

The actual steady-state value of V_{st} is a result of the evolution of the system which starts at $V_{st0} = V_{res}$. Indeed, in this experiment, the amplitude of the mass vibration and hence the value of C_t are *affected* as the charge pump increases the value V_{st}.

Fig. 7 explains the scenario of the experiment. The goal of the experiment is to measure the saturation voltage on C_{st}, when the charge pump runs without a flyback. The only role of the flyback is a periodic initialization of the circuit (setting $V_{st} = V_{res}$), after the charge pump reaches the steady-state. In order to validate the proposed analytical method, the $V_{st\ ss}$ quantity was obtained by the multiple scales method analysis, but with a very large resistive load mimicking the operation of a freely running charge pump without a flyback. Therefore, both experimental and analytical models are equivalent as they compare a generic charge pump without flyback. The external acceleration was of amplitude 0.3 g, and the frequency was swept over the range 95 Hz–155 Hz. The same experiment was repeated for different values of V_{res}.

The plot in Fig. 8 represent the value $\Delta V = V_{st\ ss} - V_{res}$. This quantity represents the increase of the V_{st} during the charge pumping. It is directly related to the energy converted by the charge pump as:
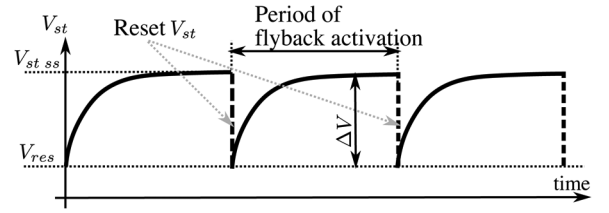
$$\Delta W = 0.5 C_{st} \Delta V^2. \tag{39}$$

Fig. 7. Description of the experiment. The charge pump was allowed to reach saturation voltage ($V_{st\ ss}$). Switched flyback was employed to reset the value of V_{st} to V_{res} once its saturation voltage was measured.
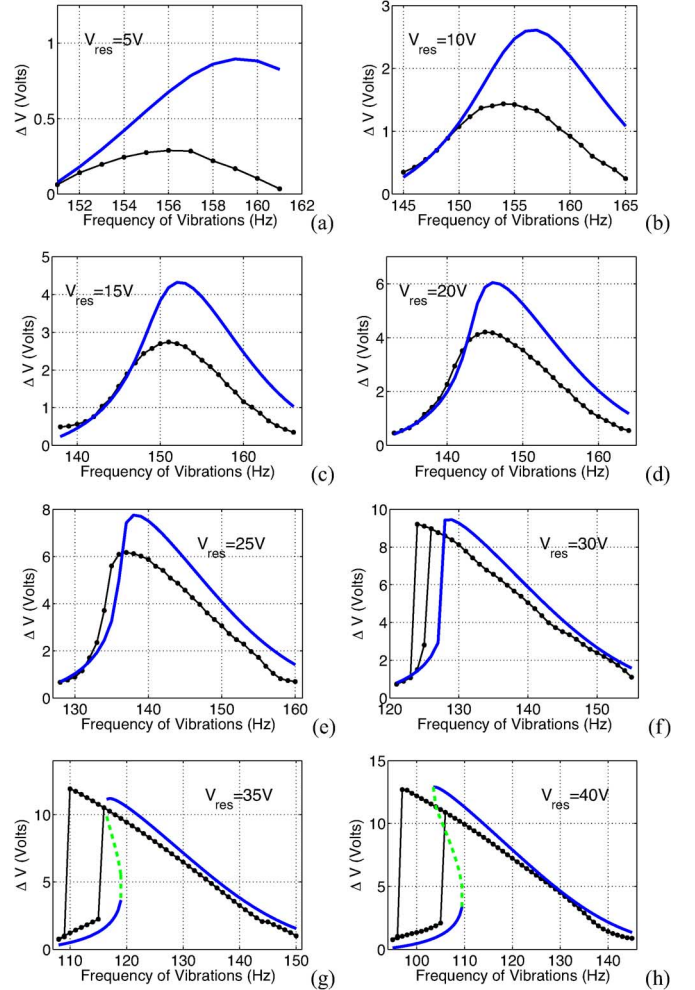

Fig. 8. The experimental $V_{st\ ss}$ values are shown by the solid black line with dots (a line is used to highlight the hysteresis effect). The solution of $V_{st\ ss}$ from the multiple scales solution (equivalent to the solution of (36)) is shown with the solid blue waveform. The green dotted line in the MSM solution highlights the hysteresis due to the multistability. Each figure represents a different initial charging voltage U_0: (a) 5 V, (b) 10 V, (c) 15 V, (d) 20 V, (e) 25 V, (f) 30 V, (g) 35 V, (h) 40 V. As the initial voltage continues to increase we see hysteresis occur.

D. Experimental Results

The ΔV obtained by the MSM is in a very good agreement with that obtained by the experiment, considering approximations used in our method (diode model, approximation about the transducer capacitance, uncertainty about the lumped parameters of the resonator). For all V_{res}, the MSM predicts a consistent frequency shift, as well as the shape of the resonance curve. It also gives quite a correct value of ΔV, in particular for moderate and large V_{res}. Tolerances of the parameters in the diodes
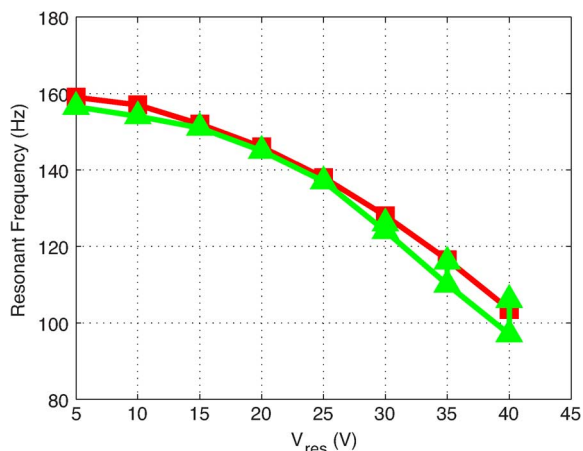
Fig. 9. A plot of the frequencies corresponding to the saturation voltage (and therefore the maximum energy on C_{st}, as shown in (39)) as a function of the initial pre-charge voltage. The green triangle waveform describes the experimental results and the red squares represent the MSM solution.

model may be a source of discrepancies at low V_{res}, since the ΔV is of the same order as the diode threshold.

It is remarkable that the nonlinear effect of the electrostatic force is prominent on the plots for large V_{res}. Indeed, hysteresis in the resonance curves can be seen both in the analytical and experimental data. At increased V_{res}, the MSM solution shows the existence of two stable branches joined by a third unstable branch. The reproduction of the hysteresis in the MSM solutions is interesting as it highlights the nonlinearity is due to electrical, and not mechanical, forces. As noted previously in Section III, if the Routh-Hurwitz criterion is not satisfied a saddle orbit exists. For the unstable branch, in the area of the hysteresis, the Routh-Hurwitz criterion is indeed negative and so we can deduce the presence of a saddle orbit.

Fig. 9 provides a global view of the resonance frequency shift as V_{res} voltage increases, where experimental data is compared with results from the MSM model. This shows good agreement of the method (36) proposed in Section V with the experimental modification of frequency due to electromechanical coupling.

VII. Conclusions

This work is the first fundamental study of the shift in resonance due to electromechanical coupling for a complex conditioning circuit employing electrostatic vibration energy conversion. It is also one of the first studies to provide an analysis of the nonlinearities arising from the electromechanical coupling of an experimental device, particularly in the case of a multi-variable conditioning circuit such as the charge pump circuit. The charge pump is a very promising eKEH conditioning circuit. While in this work we have modelled a charge pump with resistive flyback, both Part 1 and Part 2 have highlighted the ability to relate both flyback configurations equally by calculating an effective resistance. In terms of the electromechanical coupling behavior present in all eKEHs, the coupling is simply a function of the charge and voltage on the variable capacitor. Therefore this analysis is not simply applicable to the charge pump but to any conditioning circuits implementing a rectangular QV cycle, such as Bennet's doubler.

The electromechanical coupling due to the force f_t is the cause of all the nonlinearities in the system. The influences of the nonlinear coupling described in this work include:

- The amplitude of the resonator displacement is directly affected by the magnitude of the attractive force between the capacitor plates.
- The resonant frequency of oscillations can shift due to the electromechanical coupling, this also effects the amplitude of oscillations in the resonator.
- The change in resonator dynamics such as a cascade of bifurcations, shown in Fig. 5.

The necessity in gaining an enhanced understanding of the entire system in order to truly optimize the energy harvested by these devices is highlighted experimentally in Fig. 8. Even at low electrostatic biasing the maximum energy is not harvested at the resonance frequency. As shown in Fig. 6, there is no way to determine what shift may occur for different transducers and parameter values without modelling the nonlinear coupling. Therefore we simply cannot afford to neglect the influence of the transducer force and the nonlinearities it introduces.

The model resulting from the multiple scales method can be relatively easily adapted to include mechanical nonlinearities [21]. Therefore, from this work, it is envisaged that we will be able to expand this analysis to include further nonlinear influences such as white noise and mechanical nonlinearities as a potential route to widening the systems frequency response [23]–[26].

Simulations of the differential equations describing the resonator and conditioning circuitry compare very accurately with the corresponding VHDL-AMS/ELDO results. The models presented in this study have been compared with novel experimental results and provide a greater understanding of the electromechanical coupling which resulted in the experimental data.

References

[1] P. Mitcheson, E. Yeatman, G. Rao, A. Holmes, and T. Green, "Energy harvesting from human and machine motion for wireless electronic devices," *Proc. IEEE*, vol. 96, no. 9, pp. 1457–1486, 2008.
[2] S. Roundy, P. K. Wright, and J. Rabaey, "A study of low level vibrations as a power source for wireless sensor nodes," *Comput. Commun.*, vol. 26, no. 11, pp. 1131–1144, Jul. 2003.
[3] S. Meninger, J. Mur-Miranda, R. Amirtharajah, A. Chandrakasan, and J. Lang, "Vibration-to-electric energy conversion," *IEEE Trans. Very Large Scale Integr. (VLSI) Syst.*, vol. 9, no. 1, pp. 64–76, 2001.
[4] E. Torres and G. Rincon-Mora, "Electrostatic energy-harvesting and battery-charging cmos system prototype," *IEEE Trans. Circuits Syst. I, Reg. Papers*, vol. 56, no. 9, pp. 1938–1948, Sep. 2009.
[5] P. Basset, D. Galayko, F. Cottone, R. Guillemet, E. Blokhina, F. Marty, and T. Bourouina, "Electrostatic vibration energy harvester with combined effect of electrical nonlinearities and mechanical impact," *J. Micromech. Microeng.*, vol. 24, no. 3, p. 035001, 2014.
[6] D. Galayko, E. Blokhina, P. Basset, F. Cottone, A. Dudka, E. O'Riordan, and O. Feely, "Tools for analytical and numerical analysis of electrostatic vibration energy harvesters: Application to a continuous mode conditioning circuit," *J. Phys., Conf. Series*, vol. 476, p. 012076, 2013, no. 1, IOP Publ..
[7] D. Galayko and P. Basset, "A general analytical tool for the design of vibration energy harvesters (vehs) based on the mechanical impedance concept," *IEEE Trans. Circuits Syst. I, Reg. Papers*, vol. 58, no. 2, pp. 299–311, 2011.
[8] J. O. Mur-Miranda, "Mems-enabled electrostatic vibration-to-electric energy conversion," Ph.D. dissertation, Massachusetts Inst. Technol., Cambridge, MA, USA, 2003.
[9] E. Blokhina, D. Galayko, P. Basset, and O. Feely, "Steady-state oscillations in resonant electrostatic vibration energy harvesters," *IEEE Trans. Circuits Syst. I, Reg. Papers*, vol. 60, no. 4, pp. 875–884, 2013.
[10] B. Yen and J. H. Lang, "A variable-capacitance vibration-to-electric energy harvester," *IEEE Trans. Circuits Syst. I, Reg. Papers*, vol. 53, no. 2, pp. 288–295, 2006.

[11] A. Dudka, D. Galayko, E. Blokhina, and P. Basset, "Smart integrated conditioning electronics for electrostatic vibration energy harvesters," in *Proc. IEEE Int. Symp. Circuits Syst. (ISCAS)*, Jun. 2014.

[12] M. A. Karami and D. J. Inman, "Equivalent damping and frequency change for linear and nonlinear hybrid vibrational energy harvesting systems," *J. Sound Vib.*, vol. 330, pp. 5583–5597, 2011.

[13] A. C. M. de Queiroz and M. Domingues, "The doubler of electricity used as battery charger," *IEEE Trans. Circuits Syst. II, Exp. Briefs*, vol. 58, no. 12, pp. 797–801, 2011.

[14] H. R. Florentino, D. Galayko, R. C. Freire, B. A. Luciano, and C. Florentino, "Energy harvesting circuit using variable capacitor with higher performance," *J. Integr. Circuits Syst.*, vol. 6, no. 1, pp. 68–74, 2011.

[15] A. Kempitiya, D. Borca-Tasciuc, and M. Hella, "Low-power interface ic for triplate electrostatic energy converters," *IEEE Trans. Power Electron.*, vol. 28, no. 2, pp. 609–614, Feb. 2013.

[16] A. Dudka, P. Basset, F. Cottone, E. Blokhina, and D. Galayko, "Wideband electrostatic vibration energy harvester (e-veh) having a low start-up voltage employing a high-voltage integrated interface," *J. Phys., Conf. Series*, vol. 476, p. 012127, 2013, no. 1, IOP Publ..

[17] F. Pêcheux, C. Lallement, and A. Vachoux, "VHDL-AMS and verilog-ams as alternative hardware description languages for efficient modeling of multidiscipline systems," *IEEE Trans. Comput.-Aided Design Integr. Circuits Syst.*, vol. 24, no. 2, pp. 204–225, 2005.

[18] A. S. Sedra and K. C. Smith, *Microelectronic Circuits*. Oxford, U.K.: Oxford Univ. Press, 1998, vol. 1.

[19] E. O'Riordan, E. Blokhina, D. Galayko, and O. Feely, "Modelling and analysis of vibration energy harvesters with charge pump conditioning circuits," in *Proc. IEEE Int. Symp. Circuits Syst. (ISCAS)*, Jun. 2014.

[20] A. Nayfeh, *Introduction to Perturbation Techniques*. New York: Wiley, 1993.

[21] E. Blokhina, D. Fournier-Prunaret, P. Harte, D. Galayko, and O. Feely, "Combined mechanical and circuit nonlinearities in electrostatic vibration energy harvesters," in *Proc. IEEE Int. Symp. Circuits Syst. (ISCAS)*, May 2013, pp. 2739–2742.

[22] A. Nayfeh and B. Balachandran, *Applied Nonlinear Dynamics*. Weinheim, Germany: Wiley-VCH, 2004.

[23] F. Cottone, H. Vocca, and L. Gammaitoni, "Nonlinear energy harvesting," *Phys. Rev. Lett.*, vol. 102, no. 8, p. 080601, 2009.

[24] E. Halvorsen, "Energy harvesters driven by broadband random vibrations," *J. Microelectromech. Syst.*, vol. 17, no. 5, pp. 1061–1071, Oct. 2008.

[25] S. C. Stanton, C. C. McGehee, and B. P. Mann, "Nonlinear dynamics for broadband energy harvesting: Investigation of a bistable piezoelectric inertial generator," *Physica D: Nonlinear Phenomena*, vol. 239, no. 10, pp. 640–653, 2010.

[26] S. D. Nguyen, E. Halvorsen, and G. Jensen, "Wideband mems energy harvester driven by colored noise," *J. Microelectromech. Syst.*, vol. 22, no. 4, pp. 892–900, Aug. 2013.

Dimitri Galayko (M'12) graduated from Odessa State Polytechnich University, Ukraine, in 1998; he received his master degree from Institut of Applied Sciences of Lyon, INSA-LYON, France, in 1999. He created his Ph.D. thesis in the Institute of Microelectronics and Nanotechnologies (IEMN), Lille, France, and received the Ph.D. degree from the University Lille-I in 2002. The topic of his Ph.D. dissertation was the design of microelectromechanical silicon filters and resonators for radiocommunications. Since 2005 he is an Associate Professor at University of Paris VI (UPMC, Sorbonne Universités), France, in the LIP6 laboratory. His research interests include study, modeling, and design of nonlinear integrated circuits for sensor interface and for mixed-signal applications.

Philippe Basset received the engineering diploma in electronic from ISEN Lille, France, in 1997, and the M.Sc and Ph.D degrees from IEMN University of Lille, France, in 1999 and 2003 respectively. In 2004 he was a Postdoc at CMU, Pittsburgh, PA, USA. In 2005 he joined ESIEE Paris at the Universit Paris-Est, France, where he is currently an Associate Professor. His research interests include micro/nano-structuration of silicon and micropower sources for autonomous MEMS. He led several projects on energy harvesting using micro- and nano-technologies and he serves in the TPC of the PowerMEMS conference since 2013. A member of the ESYCOM laboratory, he is currently leading the Sensors and Measuring MEMS group.

Orla Feely (S'85–M'86–SM'00–F'09) received the B.E. degree in electronic engineering from University College Dublin (UCD), Ireland, in 1986, and the M.S. and Ph.D. degrees in electrical engineering from the University of California, Berkeley, CA, USA, in 1990 and 1992, respectively. She joined UCD in 1992 and is currently Vice-President for Research, Innovation and Impact. Her research interests lie in the area of nonlinear dynamics of electronic circuits. Prof. Feely is a Fellow of Engineers Ireland and the Irish Academy of Engineering. She received the Best Paper Awards of the International Journal of Circuit Theory and Applications, 2007, and the European Conference on Circuit Theory and Design, 1997. Her Ph.D. thesis won the D. J. Sakrison Memorial Prize for outstanding and innovative research, awarded annually by the Department of Electrical Engineering and Computer Science, U. C. Berkeley. She serves/has served on the Editorial Boards of the IEEE TRANSACTIONS ON CIRCUITS AND SYSTEMS and the *International Journal of Circuit Theory and Applications*, and as Chair of the IEEE Technical Committee on Nonlinear Circuits and Systems. Prof. Feely is Chair of the Irish Research Council.

Eoghan O'Riordan received the B.E. degree in electrical engineering from University College Dublin (UCD), Ireland, in 2012. He is currently working toward a Ph.D. degree in electronic engineering at UCD. His research interests include nonlinear dynamics, and vibration energy harvesting.

Elena Blokhina (S'05–M'06–SM'13) received the M.Sc. and Ph.D. degrees in physics from Saratov State University, Saratov, Russia, in 2002 and 2005, respectively. From 2005 to 2007, she was a Research Scientist at Saratov State University, where she worked in the area of analysis and modeling of microwave electron devices. Since 2007, she has been with University College Dublin, Dublin, Ireland, where she currently is a lecturer and the research manager of the Circuits and Systems Research Group. Her research interests include nonlinear dynamics and oscillation theory and their application to the analysis of MEMS and energy harvesters. Dr. Blokhina is a member of the IEEE Technical Committee on Nonlinear Circuits and Systems. She has been elected to serve in the Board of Governors of the IEEE Circuits and Systems society for the term 2013–2015. She has served as a reviewer and review committee member for a number of international journals and conferences on circuits and systems, nonlinear dynamics and numerical modelling. She has served as the track co-chair for Nonlinear Circuits and Systems, Neural Networks at the IEEE International Conference on Electronics, Circuits and Systems (2013 and 2014) and the track chair for Nonlinear Circuits and Systems at the IEEE International Symposium on Circuits and Systems (2015).

Andrii Dudka received the M.S. degree in computer science and electronics from Odessa National Polytechnic University, Ukraine, in 2008, and the Ph.D. degree in electrical engineering from the Pierre and Marie Curie University, lab. LIP6, France, in 2014. He is currently a Postdoctoral Researcher at University of Bordeaux, lab. IMS, France. His research interests are in the areas energy harvesting from vibrations, micropower generation and conversion using MEMS devices, analog electronics, and ASICs.